PHYSICAL REVIEW B **97**, 094307 (2018)

Saturation and negative temperature coefficient of electrical resistivity in liquid iron-sulfur alloys at high densities from first-principles calculations

Fabian Wagle and Gerd Steinle-Neumann
Bayerisches Geoinstitut, Universität Bayreuth, 95440 Bayreuth, Germany

Nico de Koker
School of Geosciences, University of the Witwatersrand, Private Bag 3, 2050 Wits, South Africa

(Received 17 January 2018; published 28 March 2018)

We report results on electronic transport properties of liquid Fe-S alloys at conditions of planetary cores, computed using first-principle techniques in the Kubo-Greenwood formalism. We describe a combined effect of resistivity saturation due to temperature, compression, and chemistry by comparing the electron mean free path from the Drude response of optical conductivity to the mean interatomic distance. At high compression and high sulfur concentration the Ioffe-Regel condition is satisfied, and the temperature coefficient of resistivity changes sign from positive to negative. We show that this happens due to a decrease in the *d* density of states at the Fermi level in response to thermal broadening.

DOI: 10.1103/PhysRevB.97.094307

I. INTRODUCTION

An understanding of the stability of planetary magnetic fields and the thermal evolution of terrestrial planets is closely related to the characterization of electronic transport properties of liquid Fe and Fe alloys that make up the dynamo-active portions of their cores. Recent years have seen significant progress in this direction, and both electrical (σ) and thermal (λ_{th}) conductivities have been determined at high pressure P and high temperature T by means of *ab initio* simulations [1–3] and experiments [4–8]. While a consensus has emerged that σ at conditions of planetary cores is significantly higher than previously thought [9,10], there is considerable controversy on values of λ_{th} [1–3,11,12] that includes a discussion of the validity of the Wiedemann-Franz law that relates both electronic transport quantities.

For the Earth's core, Fe is likely alloyed with silicon and/or oxygen [13,14], which have therefore been the focus of previous studies [1,3–5]. By contrast, in the cores of Mercury and Mars, sulfur is expected to be the dominant light element alloying with iron [15,16]: It is cosmically abundant and shows a high solubility in liquid iron due to its compatibility in electronic structure and the similar atomic size of Fe and S [17,18]. In the Earth's core, sulfur is unlikely to play an important role as the giant Moon-forming impact has probably led to the loss of this moderately volatile element [19].

The observed decrease in conductivity ($\sigma \propto 1/T$) of liquid metals in experiments [20,21] and computations, also at high P [1], is consistent with the Bloch-Grüneisen law for solids above the Debye temperature θ_D that describes the shortening of the electron mean free path $x_{\mathrm{eff}} \propto 1/T$. In the quasi-free-electron model, scattering events in the liquid occur due to the interaction of electrons with atomic potentials [22]. For this scattering mechanism, the interatomic distance sets a lower bound for the mean free path, which is known as the Ioffe-Regel condition [23], leading to saturation. Resistivity saturation has been found to be an important factor in highly resistive transition metals and their alloys [24], in which x_{eff} is already short due to the following static and dynamic effects:

(i) Experiments at ambient P reveal that a high concentration of impurities can shorten x_{eff} sufficiently since the alloying element introduces compositional disorder [25]. Chemically induced saturation continues to take place at high P, as has been shown for the Fe-Si-Ni system [6]. Gomi *et al.* [6] combined diamond-anvil-cell experiments with first-principles calculations and showed that Matthiessen's rule [26] breaks down close to the saturation limit.

(ii) Increasing thermal disorder also induces saturation, as has been demonstrated by analyzing the temperature coefficient of resistivity (TCR) in NiCr thin films [25]. Recent computations [27] observe a sublinear trend of $\rho(T) = 1/\sigma$ for hexagonal close packed (hcp) iron at P of the Earth's inner core.

(iii) In addition to impurities and T, pressure can lead to saturation. This has been shown for the Fe-Si system in the multi-anvil press [28].

Since electrical conductivity measurements of liquid iron and its alloys at conditions of the Earth's core are challenging [29], high-P studies extrapolate ambient-T [5,8] or high-T experiments [7] for the solid to the melting temperature and the liquid phase, accounting for saturation by a parallel resistor model. The extrapolation of their models supports low values of ρ for the Earth's core, consistent with computational studies [1–3]. Here, we investigate the electronic transport properties for liquid iron-sulfur alloys based on first-principles simulations to complement the existing results for Fe [1,2] and the Fe-O-Si system [1,3] and to compare to recent experiments in the Fe-Si-S system [8]. The first-principles approach also provides the opportunity to explore resistivity saturation in terms of the Ioffe-Regel condition and the TCR by means of the electronic structure.

II. METHODS

We generate representative liquid configurations using density-functional-theory-based molecular dynamics (DFT-MD) simulations, for which we then perform electronic linear response calculations to obtain transport properties.

A. Molecular dynamics simulations

DFT-MD simulation cells contain 128 atoms, and the calculations are performed in the N-V-T ensemble using the plane-wave code VASP [30–32]. Cubic cells in a volume range between 7.09 and 11.82 $\mathring{A}^3$/atom (six equally spaced volumes, covering the P range of the Earth) and sulfur contents of 12.5 (Fe_7S) and 25 at % (Fe_3S; ∼7.6 and ∼16 wt %) are set up by randomly replacing Fe atoms in molten configurations from previous simulations [1]. At 8.28 $\mathring{A}^3$/atom we also set up $Fe_{15}S$ and $Fe_{27}S_5$ compositions to consider the dependence of resistivity on composition in more detail. Atomic coordinates are updated using a time step of 1 fs, and T is controlled by the Nosé thermostat [33], with T between 2000 and 8000 K. At each time step, the electron density is computed using the projector augmented-wave (PAW) method [34] with the Perdew-Burke-Ernzerhof exchange-correlation functional [35] and a plane-wave cutoff energy of 400 eV. Electronic states are occupied according to Fermi-Dirac statistics at T of the thermostat. Brillouin zone sampling is restricted to the zone center. After equilibration of P, T, and the total energy E is achieved (typically after a few hundred femtoseconds), the DFT-MD simulations are continued for at least 15 ps.

B. Resistivity calculations

The kinetic coefficients in linear response to an electric field $\mathbf{E}$ and a thermal gradient ∇T build up the Onsager matrix $\mathcal{L}_{ij}$ [36],

$$\mathbf{j}_{\mathrm{el}} = \mathcal{L}_{11}\mathbf{E} + \mathcal{L}_{12}\nabla T, \tag{1}$$

$$\mathbf{j}_{\mathrm{th}} = \mathcal{L}_{21}\mathbf{E} + \mathcal{L}_{22}\nabla T, \tag{2}$$

where $\mathbf{j}_{\mathrm{el}}$ and $\mathbf{j}_{\mathrm{th}}$ are electrical and thermal current densities, respectively. Electrical conductivity and the electronic contribution to thermal conductivity are then

$$\sigma = \mathcal{L}_{11} \tag{3}$$

and

$$\lambda_{\mathrm{th}}^{\mathrm{el}} = \frac{1}{e^2 T}\left(\mathcal{L}_{22} - \frac{\mathcal{L}_{12}^2}{\mathcal{L}_{11}}\right). \tag{4}$$

We extract at least six uncorrelated snapshots from the MD simulations (i.e., separated by time periods greater than that required for the velocity autocorrelation function to decay to zero) and compute Kohn-Sham wave functions ψ_k, their energy eigenvalues ϵ_k, and the Cartesian gradients of the Hamiltonian with respect to a shift in wave vector $\partial\mathcal{H}/\partial\mathbf{k}$ using the ABINIT software package [37–39]. From those, the frequency-dependent Onsager matrix elements are calculated with the Kubo-Greenwood equations,

$$\mathcal{L}_{ij} = (-1)^{i+j}\frac{\hbar e^2}{V_{\mathrm{cell}}}\sum_{k',k}[f(\epsilon_{k'}) - f(\epsilon_k)]\delta(\epsilon_{k'} - \epsilon_k - \hbar\omega) \times \langle\psi_k|\hat{\mathbf{v}}|\psi_{k'}\rangle\langle\psi_{k'}|\hat{\mathbf{v}}|\psi_k\rangle(\epsilon_{k'} - \mu_e)^{i-1}(\epsilon_k - \mu_e)^{j-1}, \tag{5}$$

as implemented in the CONDUCTI module of ABINIT [40]. In Eq. (5), $\hbar$ denotes the reduced Planck constant, e is the elementary charge, V_{cell} is the cell volume, ω is the frequency of the external field, $\hat{\mathbf{v}} = 1/\hbar \cdot \partial\mathcal{H}/\partial\mathbf{k}$ is the velocity operator, and μ_e is the electronic chemical potential.

By fitting the Drude formula for optical conductivity

$$\Re[\sigma(\omega)] = \frac{\sigma_0}{1 + (\omega\tau)^2} \tag{6}$$

to the Kubo-Greenwood results for each snapshot, we extract the dc limit of conductivity σ_0 (used without subscript elsewhere) and effective relaxation time τ. Thermal conductivity is extrapolated linearly to the limit $\omega \to 0$ over a $\hbar\omega$ range of 2 eV. We average σ, τ, and λ_{th} over the snapshots and take one standard deviation as uncertainty. Calculations with denser grids of $2 \times 2 \times 2$ and $3 \times 3 \times 3$ k points show that $\sigma(\omega)$ is sufficiently converged (to within 3%) in calculations using a single k point (see Fig. S1 in the Supplemental Material [41]).

The resulting $\rho(V,T)$ and $\lambda_{\mathrm{th}}(V,T)$ are fit with a physically motivated closed expression (Appendix A) to interpolate between results and extrapolate to conditions not investigated.

C. Electron density of states

We compute the site-projected and angular-momentum-decomposed electron densities of states (DOSs) with the tetrahedron method [42,43], using a nonshifted $2 \times 2 \times 2$ k-point grid with small energy increments of 1.4×10^{-3} eV. The radii of the atomic spheres, in which the angular-momentum projections are evaluated, have been chosen to be space filling and proportional to the radii of the respective PAW spheres [34]. The DOS is computed for the same snapshots as those used for the evaluation of the Kubo-Greenwood equations and re-binned with an energy window of $\sim 1/2k_BT$ to resolve T-dependent features in the vicinity of the Fermi energy E_F. This results in a strongly varying DOS which is independent of the smearing parameter.

III. RESULTS AND DISCUSSION

A. Electrical resistivity

For the low-impurity composition Fe_7S, we find a dependence of ρ on V and T similar to that predicted in previous studies on pure Fe, Fe-Si, and Fe-O systems [1] (Fig. 1 and Tables S1 and S2 in the Supplemental Material [44,45]). Resistivity increases with V and T and can be reasonably well described by a linear T dependence above Θ_D (∼1000 K at low compression based on the equation-of-state parameters; see Appendix B and Table S3 in the Supplemental Material [46]), consistent with Bloch-Grüneisen theory. With decreasing V, Θ_D increases based on the thermodynamic parameters from our DFT-MD simulation, and values for ρ

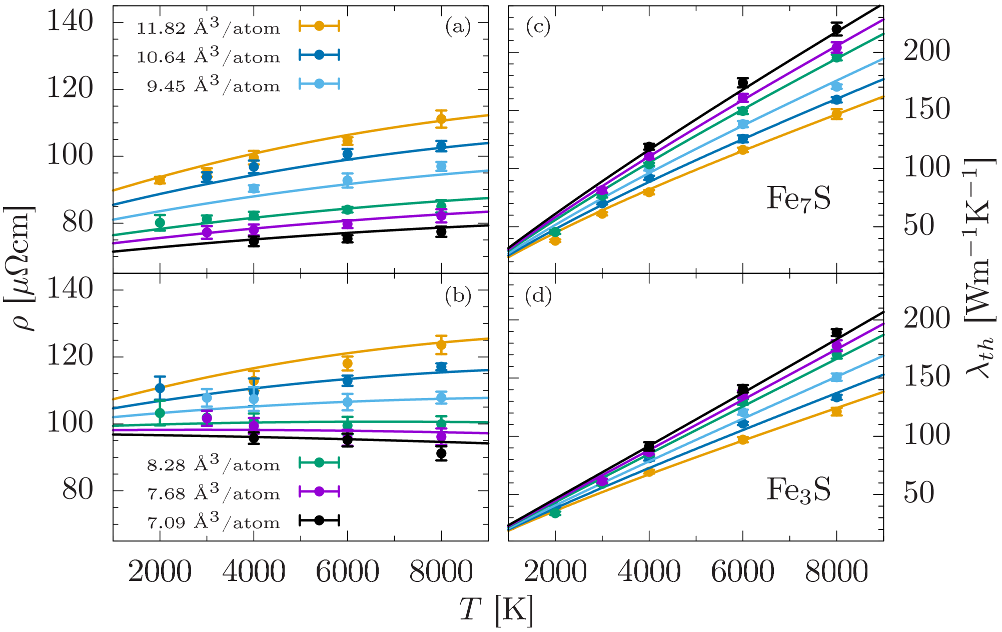

FIG. 1. Electronic transport properties of liquid Fe-S alloys as a function of temperature. The temperature coefficient of electrical resistivity of liquid (a) Fe_7S and (b) Fe_3S decreases with compression due to saturation. For Fe_3S, the temperature coefficient of resistivity becomes negative along the smallest V isochores. Solid lines represent the best fit of Eq. (A1) to resistivity. The electronic contribution to thermal conductivity of liquid (c) Fe_7S and (d) Fe_3S. Solid lines have been calculated from the best fits to $\rho(V,T)$ [Eq. (A1)] and the effective Lorenz number $L(V,T)$ [Eq. (A5)]. Tabulated values for ρ, λ_{th}, and L are given in Tables S1 and S2 in the Supplemental Material [44,45].

decrease. This behavior is well captured with the resistivity model in Appendix A.

Absolute resistivities for both compositions in the Fe-S system are similar to those for Fe-Si with the same light-element concentration [1] and higher than those for pure Fe and in the Fe-O system [1,2]. This is in contrast to experimental work [8] that estimated ρ for the solid phase in a ternary Fe-Si-S system and calculated the S impurity resistivity by using Matthiessen's rule based on previous experimental results for Fe [7] and Fe-Si [6]. Suehiro *et al.* [8] find that the influence of S on resistivity is significantly less than that of Si [6]. The experiments had to rely on this indirect determination of resistivity reduction due to sulfur, as S is hardly soluble in solid Fe at ambient P, and it is therefore difficult to synthesize a homogeneous phase as a starting material in experiments [47–50]. Further, Matthiessen's rule, applied in the analysis of the data, does not hold for systems with saturated resistivity [6].

For higher sulfur concentration, we find that ρ increases (Fig. 1; see Fig. S2 in the Supplemental Material [51]) and that the Bloch-Grüneisen behavior breaks down. The temperature coefficient of resistivity decreases with compression, up to the extreme case where it changes sign and becomes negative for Fe_3S at the smallest two volumes we consider.

Negative TCRs have been observed for liquid and amorphous solid metals, for which the maximum momentum change of a scattered electron $2k_F$ falls in the region close to the principle peak of the structure factor $S(q)$, as in the case of metals with two valence electrons, e.g., Eu, Yb, and Ba with a $6s^2$ valence configuration [52], and Cu-Zr metallic glasses [53]. It is one of the great successes of Ziman theory for the resistivity of liquid metals [22,54] to explain the negative TCR in these systems. Ziman theory cannot account for the negative TCR that we predict for Fe_3S at high compression. Because for iron and the other Fe alloys considered by de Koker *et al.* [1] $2k_F$ is near the first minimum in $S(q)$ (Fig. S3 in the Supplemental Material [55]), thermal broadening of the structure factor will lead to positive TCR over the entire compression range. This suggests that the negative TCR is a secondary effect, driven by changes in electronic structure (Sec. III C) that are only noticeable once resistivity saturation is reached by compression and impurities simultaneously.

B. Mean free path

In order to understand the effect of resistivity saturation from a semiclassical picture of electron transport, we calculate the effective electron mean free path as $x_{\text{eff}} = v_F\tau$, where $v_F = (\hbar/m)(3\pi^2 n_{\text{eff}})^{1/3}$ is the Fermi velocity, $n_{\text{eff}} = (m\sigma)/(e^2\tau)$ is the effective number density of conduction electrons, and m is the electron mass. Figure 2 reveals three distinctive features:

(i) For ambient P volumes ($V = 11.82\,\text{Å}^3$/atom), x_{eff} approaches the mean interatomic distance asymptotically with increasing T, consistent with dynamic resistivity saturation [25,27].

(ii) At the lowest cell V considered ($V = 7.09\,\text{Å}^3$/atom), the T dependence of x_{eff} vanishes within uncertainty. In addition, x_{eff} becomes shorter than at lower compression due to the increased density of scattering centers. At first glance, this observation appears to be inconsistent with the fact that ρ decreases with compression but can be understood in terms of electronic structure (Sec. III C).

(iii) With increasing sulfur concentration, x_{eff} decreases significantly. This reflects the expected behavior of an increased probability of impurity-caused scattering.

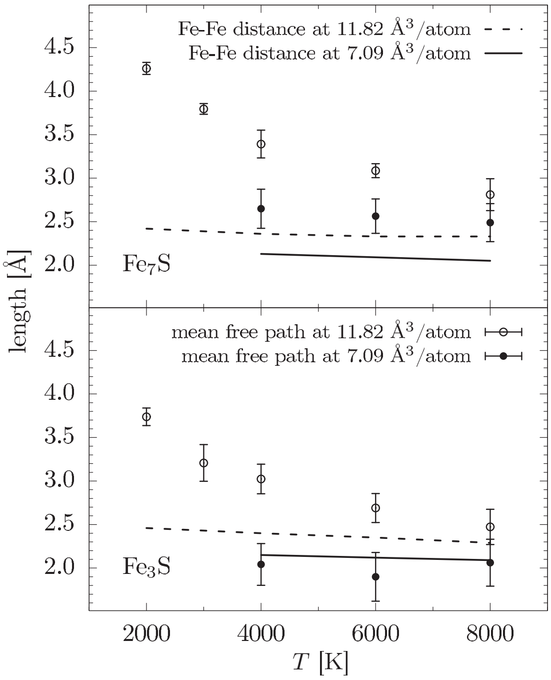

FIG. 2. Electron mean free path for liquid Fe_7S (top) and Fe_3S (bottom) for two cell volumes (near ambient P and largest compression) as a function of temperature, obtained by a Drude fit to optical conductivity [Eq. (6)]. The mean free path approaches the interatomic distance (solid lines, first peak position of the partial radial distribution function) with increasing compression and impurity concentration. For Fe_3S at the smallest cell volume, the Ioffe-Regel condition is reached.

For the highest compression the Ioffe-Regel condition is reached for Fe_3S as x_{eff} becomes equal to the mean interatomic distance within uncertainty.

C. Electronic structure

Most of the electric current in transition metals is transported by s electrons, which can scatter into d states with a far lower Fermi velocity [56]. Partially filled d bands with a high DOS at the Fermi level lead to a high probability of s-d scattering events, which dominate resistivity over s-s processes [57].

Site-projected and angular-momentum-decomposed local densities of states (LDOSs) show similar changes in response to compression and T (Figs. S4 and S5 of the Supplemental Material [58,59]). Generally, peaks broaden, and the Fe d LDOS at E_F decreases, resulting in fewer states available for s electrons to scatter into. The response of the electronic structure to compression is a dominant feature as dispersion of electronic bands increases significantly due to stronger interactions [60] (Fig. S4 in the Supplemental Material [58]).

For increasing T, changes in the DOS are less pronounced (Fig. S5 in the Supplemental Material [59]) and reflect dynamic short-range changes in the liquid structure that can lead to smaller interatomic distances [61] that are also expressed by thermal pressure [27]. This is a small effect, and the negative TCR can be observed only when compression and chemical saturation in the system have been reached.

Electronic states of iron dominate the DOS of the liquid Fe-S alloys near E_F. The densities of states for Fe and Fe_3S are quite similar at the same V and T (Figs. S4 and S5 in the Supplemental Material [58,59]), and the broadenings in the vicinity of E_F due to compression and T, respectively, are almost identical. Therefore, sulfur contributes to the overall resistivity behavior in the Fe-S systems only by shortening x_{eff} through impurity scattering, as discussed in Sec. III B (Fig. 2). In comparison to silicon and oxygen, sulfur appears to be more efficient in doing so due to its similar atomic size and the efficient bonding with iron, resulting in high Fe-S coordination numbers [17].

D. Thermal conductivity

Since lattice vibrations play only a minor role in heat transport through metals, the electronic contribution to thermal conductivity $\lambda_{\mathrm{th}}^{\mathrm{el}}$ represents total conductivity λ_{th} to a good approximation [26]. Similar to the results for ρ, we find the Kubo-Greenwood values for λ_{th} (Fig. 1) to be consistent with the ones for liquid Fe-Si alloys and somewhat larger than those of Fe-O liquids from previous computations with the same light-element concentrations [1]. Contrary to electrical resistivity, we do not see any sign of saturation in λ_{th}, putting the validity of the Wiedemann-Franz law with a constant value of the Lorenz number $L_0 \approx 2.44\ \mathrm{W}\Omega/\mathrm{K}^2$ from Drude-Sommerfeld theory in question. Indeed, thermal conductivity is significantly overestimated by using L_0 and the resistivity model (Appendix A) compared to the values computed directly with the Kubo-Greenwood equations [Eq. (5)].

Recently, electron-electron scattering has been suggested to contribute significantly to λ_{th} of hcp iron at high P but not to ρ [12], an effect that is ignored in the independent electron approximation of the Kubo-Greenwood approach. However, it remains an open question to what degree this contribution affects thermally disordered systems. Electronic transport critically depends on the electronic structure at the Fermi level, which is quite different for a high-density liquid at high T compared to a perfect crystal. Until the influence of electron-electron scattering on transport properties of disordered $3d$ transition metals and their alloys is better understood, values for λ_{th} from the Kubo-Greenwood approach should be used with caution.

E. Application to planetary interiors

We convert resistivity values and fits in V-T space (Appendix A and Table I) to $\rho(P,T)$ by using the self-consistently obtained equations of state for Fe_7S and Fe_3S (Appendix B and Fig. S6 and Table S3 in the Supplemental Material [46,62]). Resistivity values for Fe_7S and Fe_3S (Fig. 3) are substantially larger than the corresponding ones for pure iron. While resistivities for Fe_7S along different isotherms continue to show distinctive P trends, they become indistinguishable for Fe_3S at high P due to the combined saturation effects discussed in Sec. III B. For Fe_3S, resistivity saturates at $\sim 100\ \mu\Omega\,\mathrm{cm}$, a value which remains approximately constant and T independent over the P range of the Earth's outer core, similar to the behavior of Fe_3Si [1].

TABLE I. Fit parameters of the models for $\rho(V,T)$ [Eqs. (A2)–(A4)] and $L(V,T)$ [Eq. (A5)] for liquid Fe, Fe_7S, and Fe_3S. Uncertainties of the fit parameters are large and exceed their values in most cases.

	Fe	Fe_7S	Fe_3S
ρ_{0R} ($\mu\Omega$ cm)	75.10	89.03	105.2
ρ_{1R} ($\mu\Omega$ cm)	21.48	12.73	12.06
a	0.792	0.389	0.124
b	1.479	1.804	2.686
c ($\mu\Omega$ cm)	747.2	2077	6609
d ($\mu\Omega$ cm)	1405	2829	2910
L_R (W Ω/K^2)	2.005	2.105	1.991
e	−0.097	−0.106	−0.228
f	0.041	−0.027	−0.022

There is a large discrepancy between our results and the high-T extrapolation of experimental resistivity [8] reported along model adiabats in the cores of Mars and the Earth [49,63]. Despite the similar compositions between the work presented here and the experiments (which fall between Fe_3S and Fe_7S, towards the higher sulfur concentration), the experimental profile for Earth's core shows significantly lower values, more consistent with the Kubo-Greenwood results for pure Fe [1,2]. Model values of Suehiro *et al.* [8] in the P range of the Martian core are closer to our results (Fig. 3), but the slope $(\partial\rho/\partial P)_S$ in the model based on experiments is significantly larger than in our work.

A small contribution to the difference between the experimental data and our results may come from the fact that the experiments have been performed for the solid and the simulations for the liquid, and resistivity increases discontinuously across the melting point for metals and their alloys at both ambient [64] and high P [65–68]. However, based on the Ziman approximation [22], this difference is expected to decrease with P if the density and compressibility of the coexisting solid and liquid phases become more similar. For pure iron, for example, this discontinuity is likely to become negligible at conditions of the Earth's core [69]. Rather than the difference decreasing with P as expected, it increases between the experimental data [8] and our computational results (Fig. 3).

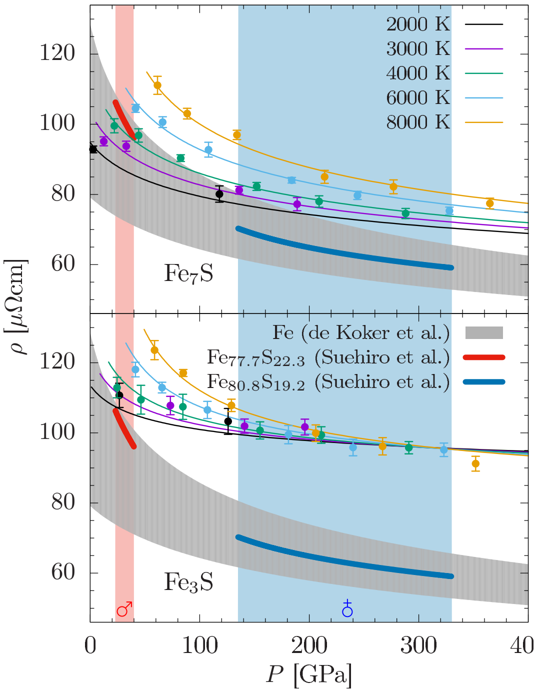

FIG. 3. Electrical resistivity of liquid Fe-S alloys as a function of pressure for Fe_7S (top) and Fe_3S (bottom). Solid lines are best fits of a parallel-resistor model to $\rho(V,T)$ [Eq. (A1)] converted from V-T to P-T conditions using the equation-of-state fits (Appendix B). Results from an experimental study [8] along a model areotherm (red line) and geotherm (blue line) as well as computational results for pure Fe [1] between 2000 and 8000 K (gray area) are included for comparison.

IV. CONCLUSIONS

We presented electronic transport properties of liquid Fe-S alloys from DFT-MD simulations at conditions relevant for the cores of terrestrial planets. We find absolute values of electrical resistivity and thermal conductivity to be consistent with those of other Fe-light-element alloys reported in previous work [1,70], ranging from 75 to 125 $\mu\Omega$ cm and 30 to 220 W m^{-1} K^{-1}. Fe alloys with low S content exhibit a positive TCR along isochores, which gradually decreases upon compression. We show that this is due to a compression-induced resistivity saturation by comparing the electron mean free path to interatomic distances. For high S concentrations (Fe_3S), the mean free path is further shortened by increased impurity scattering, sufficient to reach the Ioffe-Regel condition at the lowest volumes, resulting in a saturation of resistivity. At these conditions the TCR becomes negative, which is caused by a decrease in the Fe d density of states at the Fermi level.

For applications in planetary physics, we provide models for $\rho(V,T)$ and $\lambda_{\mathrm{th}}(V,T)$ (Appendix A), which, in combination with a self-consistent thermodynamic equation of state (Appendix B), can be translated to the P-T conditions of planetary cores.

ACKNOWLEDGMENTS

This work was supported by the Deutsche Forschungsgemeinschaft (German Science Foundation, DFG) in the Focus Program "Planetary Magnetism" (SPP 1488) with Grant No. STE1105/10-1 and Research Unit "Matter under Planetary Interior Conditions" (FOR 2440) with Grant No. STE1105/13-1. Computing and data resources for the current project were provided by the Leibniz Supercomputing Centre of the Bavarian Academy of Sciences and the Humanities. We greatly acknowledge informative discussions with V. Recoules and M. Preising on the electron density-of-states evaluation and helpful comments by an anonymous reviewer.

APPENDIX A: MODEL FOR ELECTRICAL AND THERMAL CONDUCTIVITY

We describe the resistivity behavior $\rho(V,T)$ with a parallel-resistor model:

$$\frac{1}{\rho(V,T)} = \frac{1}{\rho_{\mathrm{BG}}(V,T)} + \frac{1}{\rho_{\mathrm{sat}}(V)} + \frac{1}{\rho_{\mathrm{el}}(T)}, \tag{A1}$$

where

$$\rho_{\mathrm{BG}} = \rho_0 \left(\frac{V}{V_0}\right)^a + \rho_1 \left(\frac{V}{V_0}\right)^b \frac{T}{T_0} \tag{A2}$$

is the empirical expression used by de Koker *et al.* [1] based on the Bloch-Grüneisen formula.

$$\rho_{\mathrm{sat}} = c\left(\frac{V}{V_0}\right)^{\frac{1}{3}} \tag{A3}$$

is a term accounting for resistivity saturation, and

$$\rho_{\mathrm{el}} = d\frac{T_0}{T} \tag{A4}$$

describes the effect of thermal broadening of the DOS. The assumptions entering equations (A1)–(A4) are as follows:

(i) Sources of resistivity contributions in Eq. (A1) are independent, and therefore, conductivities are additive.

(ii) In the limit of high T, the Bloch-Grüneisen formula is linear in T. Both residual resistivity [first term in Eq. (A2)] and the material-dependent prefactor of the second term are well described by a power law in V/V_0.

(iii) Saturation resistivity [Eq. (A3)] is proportional to interatomic distance and therefore increases $\propto (V/V_0)^{1/3}$. This is consistent with the saturation resistivities for pure Fe reported by Ohta *et al.* [7].

(iv) Since the effect of thermal broadening on the DOS at E_F can be attributed to a resistivity contribution due to thermal pressure (Fig. S5 in the Supplemental Material [59]), we describe ρ_{el} in Eq. (A4) as inversely proportional to T.

Rather than fitting a model for λ_{th} directly, we compute an effective Lorenz number L at each simulation and fit $L(V,T)$ as [1]

$$L(V,T) = L_R \left(\frac{V}{V_0}\right)^e \left(\frac{T}{T_0}\right)^f. \tag{A5}$$

Fit parameters are listed in Table I.

APPENDIX B: EQUATION-OF-STATE MODEL

In order to describe electronic transport properties as a function of P suitable for comparison to experiments and for applications in planetary models, we fit a thermodynamic model to the Fe_7S and Fe_3S results that is based on a separation of the Helmholtz energy in an ideal gas, electronic and excess term [71,72]. The volume dependence of the excess term is represented by Eulerian finite strain f with the exponent $n = 2$ and a similarly reduced T term Θ with the exponent $m = 0.79$ and expansion orders $\mathcal{O}_f = 3$ and $\mathcal{O}_\Theta = 2$, parameters that describe the results for liquid iron well [1]. Figure S6 in the Supplemental Material shows the quality of the fit for E, P, and the electronic entropy S_{el} of the DFT-MD results [62]. Thermodynamic parameters at reference conditions are summarized in Table S3 of the Supplemental Material [46].

[1] N. de Koker, G. Steinle-Neumann, and V. Vlček, Proc. Natl. Acad. Sci. USA **109**, 4070 (2012).

[2] M. Pozzo, C. Davies, D. Gubbins, and D. Alfè, Nature (London) **485**, 355 (2012).

[3] M. Pozzo, C. Davies, D. Gubbins, and D. Alfè, Phys. Rev. B **87**, 014110 (2013).

[4] C. T. Seagle, E. Cottrell, Y. Fei, D. R. Hummer, and V. B. Prakapenka, Geophys. Res. Lett. **40**, 5377 (2013).

[5] H. Gomi, K. Ohta, K. Hirose, S. Labrosse, R. Caracas, M. J. Verstraete, and J. W. Hernlund, Phys. Earth Planet. Inter. **224**, 88 (2013).

[6] H. Gomi, K. Hirose, H. Akai, and Y. Fei, Earth Planet. Sci. Lett. **451**, 51 (2016).

[7] K. Ohta, Y. Kuwayama, K. Hirose, K. Shimizu, and Y. Ohishi, Nature (London) **534**, 95 (2016).

[8] S. Suehiro, K. Ohta, K. Hirose, G. Morard, and Y. Ohishi, Geophys. Res. Lett. **44**, 8254 (2017).

[9] F. D. Stacey and O. L. Anderson, Phys. Earth Planet. Inter. **124**, 153 (2001).

[10] F. D. Stacey and D. E. Loper, Phys. Earth Planet. Inter. **161**, 13 (2007).

[11] Z. Konôpková, R. S. McWilliams, N. Gómez-Pérez, and A. F. Goncharov, Nature (London) **534**, 99 (2016).

[12] L. V. Pourovskii, J. Mravlje, A. Georges, S. I. Simak, and I. A. Abrikosov, New J. Phys. **19**, 073022 (2017).

[13] K. Tsuno, D. J. Frost, and D. C. Rubie, Geophys. Res. Lett. **40**, 66 (2013).

[14] J. Badro, J. P. Brodholt, H. Piet, J. Siebert, and F. J. Ryerson, Proc. Natl. Acad. Sci. USA **112**, 12310 (2015).

[15] S. A. Hauck, J.-L. Margot, S. C. Solomon, R. J. Phillips, C. L. Johnson, F. G. Lemoine, E. Mazarico, T. J. McCoy, S. Padovan, S. J. Peale, M. E. Perry, D. E. Smith, and M. T. Zuber, J. Geophys. Res. **118**, 1204 (2013).

[16] K. Lodders and B. Fegley, Icarus **126**, 373 (1997).

[17] D. Alfè and M. J. Gillan, Phys. Rev. B **58**, 8248 (1998).

[18] K. Hirose, S. Labrosse, and J. Hernlund, Annu. Rev. Earth Planet Sci. **41**, 657 (2013).

[19] G. Dreibus and H. Palme, Geochim. Cosmochim. Acta **60**, 1125 (1996).

[20] J. B. van Zytveld, J. Phys. Colloques **41**, C8 (1980).

[21] P. D. Desai, T. K. Chu, H. M. James, and C. Y. Ho, Phys. Chem. Ref. Data **13**, 1069 (1984).

[22] J. M. Ziman, Philos. Mag. **6**, 1013 (1961).

[23] A. F. Ioffe and A. R. Regel, in *Progress in Semiconductors*, Vol. 4, edited by A. F. Gibson, F. A. Kroger, and R. E. Burgess (London: Heywood, 1960), p 237.

[24] O. Gunnarsson, M. Calandra, and J. E. Han, Rev. Mod. Phys. **75**, 1085 (2003).
[25] J. H. Mooij, Phys. Status Solidi A **17**, 521 (1973).
[26] N. W. Ashcroft and N. D. Mermin, *Solid State Physics* (Saunders College, Philadelphia, 1976).
[27] M. Pozzo and D. Alfè, SpringerPlus **5**, 256 (2016).
[28] S. Kiarasi and R. A. Secco, Phys. Status Solidi B **252**, 2034 (2015).
[29] D. Dobson, Nature (London) **534**, 45 (2016).
[30] G. Kresse and J. Hafner, Phys. Rev. B **47**, 558(R) (1993).
[31] G. Kresse and J. Furthmüller, Comput. Mater. Sci. **6**, 15 (1996).
[32] G. Kresse and J. Furthmüller, Phys. Rev. B **54**, 11169 (1996).
[33] S. Nosé, J. Chem. Phys. **81**, 511 (1984).
[34] G. Kresse and D. Joubert, Phys. Rev. B **59**, 1758 (1999).
[35] J. P. Perdew, K. Burke, and M. Ernzerhof, Phys. Rev. Lett. **77**, 3865 (1996).
[36] L. Onsager, Phys. Rev. **37**, 405 (1931).
[37] X. Gonze, Phys. Rev. B **55**, 10337 (1997).
[38] X. Gonze, B. Amadon, P.-M. Anglade, J.-M. Beuken, F. Bottin, P. Boulanger, F. Bruneval, D. Caliste, R. Caracas, M. Côté, T. Deutsch, L. Genovese, P. Ghosez, M. Giantomassi, S. Goedecker, D. R. Hamann, P. Hermet, F. Jollet, G. Jomard, S. Leroux, M. Mancini, S. Mazevet, M. J. T. Oliveira, G. Onida, Y. Pouillon, T. Rangel, G.-M. Rignanese, D. Sangalli, R. Shaltaf, M. Torrent, M. J. Verstraete, G. Zerah, and J. W. Zwanziger, Comput. Phys. Commun. **180**, 2582 (2009).
[39] M. Torrent, F. Jollet, F. Bottin, G. Zérah, and X. Gonze, Comput. Mater. Sci. **42**, 337 (2008).
[40] V. Recoules and J. P. Crocombette, Phys. Rev. B **72**, 104202 (2005).
[41] See Fig. S1 in the Supplemental Material at http://link.aps.org/supplemental/10.1103/PhysRevB.97.094307 for a convergence study of optical conductivity with respect to Brillouin zone sampling.
[42] O. Jepsen and O. K. Andersen, Phys. Rev. B **29**, 5965 (1984).
[43] G. Lehmann and M. Taut, Phys. Status Solidi B **54**, 469 (1972).
[44] See Table S1 in the Supplemental Material for ρ, λ_{th}, and L of Fe_7S as a function of V, T, and P.
[45] See Table S2 in the Supplemental Material for ρ, λ_{th}, and L of Fe_3S as a function of V, T, and P.
[46] See Table S3 in the Supplemental Material for thermodynamic parameters of Fe, Fe_7S and Fe_3S from the equation-of-state fit according to the modified thermodynamic model described in Appendix B.
[47] J. Li, Y. Fei, H. K. Mao, K. Hirose, and S. R. Shieh, Earth Planet. Sci. Lett. **193**, 509 (2001).
[48] A. Stewart, M. Schmidt, W. Westrenen, and C. Liebske, Science **316**, 1323 (2008).
[49] S. Kamada, E. Ohtani, H. Terasaki, T. Sakai, M. Miyahara, Y. Ohishi, and N. Hirao, Earth Planet. Sci. Lett. **359**, 26 (2012).
[50] Y. Mori, H. Ozawa, K. Hirose, R. Sinmyo, S. Tateno, G. Morard, and Y. Ohishi, Earth Planet. Sci. Lett. **464**, 135 (2017).
[51] See Fig. S2 in the Supplemental Material for electrical resistivity as a function of sulfur content, which includes Ref. [73].
[52] H.-J. Güntherodt, E. Hauser, H. U. Künzi, R. Evans, J. Evers, and E. Kaldis, J. Phys. F **6**, 1513 (1976).
[53] Y. Waseda and H. S. Chen, Phys. Status Solidi B **87**, 777 (1978).
[54] T. E. Faber and J. M. Ziman, Philos. Mag. **11**, 153 (1965).
[55] See Fig. S3 in the Supplemental Material for thermal broadening of the static structure factor.
[56] N. F. Mott, Proc. R. Soc. London, Ser. A **153**, 699 (1936).
[57] N. F. Mott, Philos. Mag. **26**, 1249 (1972).
[58] See Fig. S4 in the Supplemental Material for broadening of the electron density of states with decreasing cell volume.
[59] See Fig. S5 in the Supplemental Material for broadening of the electron density of states with increasing temperature.
[60] R. E. Cohen, L. Stixrude, and E. Wasserman, Phys. Rev. B **56**, 8575 (1997).
[61] P. Hunt, M. Sprik, and R. Vuilleumier, Chem. Phys. Lett. **376**, 68 (2003).
[62] See Fig. S6 in the Supplemental Material for the equation-of-state fit according to the modified thermodynamic model described in Appendix B.
[63] Y. Fei and C. Bertka, Science **308**, 1120 (2005).
[64] A. M. Rosenfeld and M. J. Stott, Phys. Rev. B **42**, 3406 (1990).
[65] R. A. Secco and H. H. Schlössin, J. Geophys. Res. **94**, 5887 (1989).
[66] R. E. Silber, R. A. Secco, and W. Yong, J. Geophys. Res. Solid Earth **122**, 5064 (2017).
[67] I. C. Ezenwa and R. A. Secco, Earth Planet. Sci. Lett. **474**, 120 (2017).
[68] I. C. Ezenwa, R. A. Secco, W. Yong, M. Pozzo, and D. Alfé, J. Phys. Chem. Solids **110**, 386 (2017).
[69] F. Wagle and G. Steinle-Neumann, Geophys. J. Int. **213**, 237 (2018).
[70] M. Pozzo, C. Davies, D. Gubbins, and D. Alfè, Earth Planet. Sci. Lett. **393**, 159 (2014).
[71] N. de Koker and L. Stixrude, Geophys. J. Int. **178**, 162 (2009).
[72] V. Vlček, N. de Koker, and G. Steinle-Neumann, Phys. Rev. B **85**, 184201 (2012).
[73] L. Nordheim, Naturwissenschaften **16**, 1042 (1928).